


FULL PAPER

Open Access



Migrating solar diurnal tidal variability during Northern and Southern Hemisphere Sudden Stratospheric Warmings

Tarique A. Siddiqui^{1*} , Jorge L. Chau¹, Claudia Stolle¹ and Yosuke Yamazaki^{2,3}

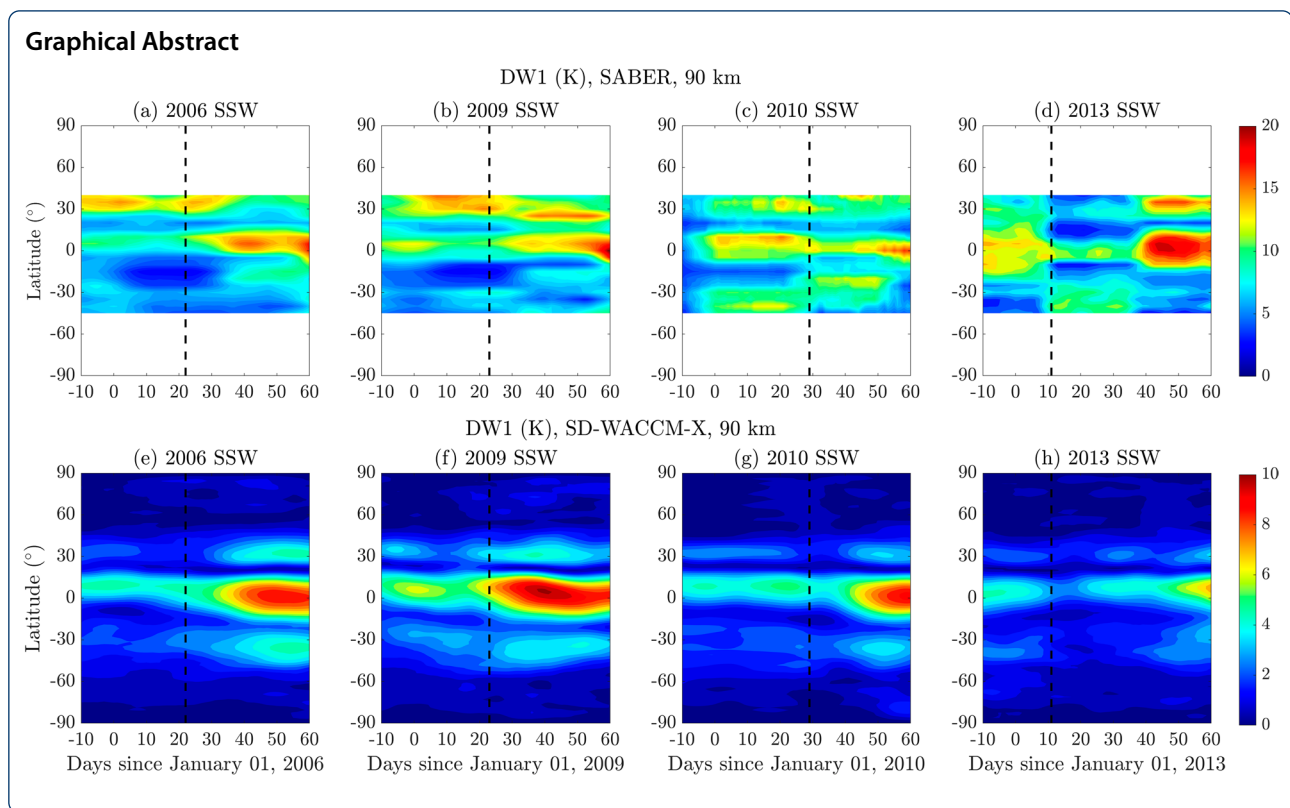
Abstract

In this study, the variability of the migrating solar diurnal (DW1) tide in the mesosphere-lower thermosphere (MLT) region during Northern and Southern Hemisphere (NH & SH) Sudden Stratospheric Warmings (SSWs) is investigated using Sounding of the Atmosphere using Broadband Emission Radiometry (SABER) temperature observations and reanalysis-driven Whole Atmosphere Community Climate Model with thermosphere and ionosphere extension (WACCM-X) simulations. The periods examined include four major NH SSWs that occurred in 2006, 2009, 2010 and 2013 and two SH SSWs that were observed in 2002 and 2019. Our analysis shows that the DW1 tide in both observations and simulations displays a reduction of amplitude at low-latitudes after the onset of NH and SH SSWs. As WACCM-X simulations qualitatively reproduce this feature of DW1 tidal variability common to both NH and SH SSWs, they have been used to examine the possible mechanism that could explain these observations in the DW1 tide. It is known that changes in the latitudinal shear of zonal winds at low-latitudes strongly affect the seasonal variation of the DW1 tide in the MLT. We show that SSW-associated changes in the latitudinal shear in the MLT could explain the observed variability of the DW1 tide during NH and SH SSWs.

Keywords: SSW, Migrating solar tide, Mesosphere-lower thermosphere (MLT), Atmospheric coupling

*Correspondence: siddiqui@iap-kborn.de

¹ Leibniz Institute of Atmospheric Physics at the University of Rostock, Kühlungsborn, Germany
Full list of author information is available at the end of the article



Introduction

Sudden stratospheric warmings (SSWs) are large-scale, transient and dynamically extreme meteorological events that are marked by a rapid rise in the polar stratospheric temperature together with the breakdown of climatological wintertime eastward winds (e.g., Scherhag 1952; Andrews et al. 1987; Baldwin et al. 2021). SSWs occur when the stratospheric polar vortex gets disrupted by the dissipation of large-scale upward propagating quasi-stationary planetary waves (QSPWs), which are forced from the troposphere (e.g., Matsuno 1971). As the eastward winds in the stratosphere act as a filter and only allow upward propagation of large-scale QSPWs with zonal wave numbers 1–3, the remaining QSPWs with higher zonal wave numbers are reflected back to the troposphere (Charney and Drazin 1961). The interaction of these upward propagating QSPWs with the stratospheric zonal mean flow results not only in the deceleration of the eastward winds but also induces a poleward flow, which descends over the polar stratosphere. The adiabatic heating associated with this descent results in the rapid rise of polar stratospheric temperature that manifests as an SSW. Depending on the extent of deceleration of the eastward zonal-mean zonal winds (ZMZW) in the polar stratosphere, SSWs are classified into ‘major’ and

‘minor’ warming events (e.g., WMO/IQSY 1964; Labitzke 1981). In the NH, a reversal of the ZMZW from eastward to westward direction at 60°N and 10 hPa has been chosen as a criteria for identifying major SSWs whereas a minor SSW is identified when there is only an increase in polar stratospheric temperature without the reversal of ZMZW (e.g., Charlton and Polvani 2007; Butler et al. 2015). In the SH, a criteria analogous to the one in the NH has been used in literature for classifying major and minor SSWs. In addition to this classification, SSWs can also be distinguished based on the morphology of the polar vortex. Depending on the zonal wavenumber of the planetary wave forcing, the stratospheric polar vortex can either get displaced off the pole or split into child vortices (e.g., Charlton and Polvani 2007). The displacement and the splitting of the polar vortex is driven predominantly by the forcing of QSPWs with wave number 1 and 2, respectively. The occurrence of SSWs are common in the Northern Hemisphere (NH) but extremely rare in the Southern Hemisphere (SH). Major SSWs occur at an average rate of six events per decade in the NH (Charlton and Polvani 2007) but in the SH, only one major SSW and one minor SSW occurring during September 2002 and 2019, respectively, have so far been observed. The inter-hemispheric asymmetry in the occurrence of SSW has

been attributed to the difference in planetary wave (PW) forcing due to orography and land-sea contrast in the two hemispheres (e.g., Waugh and Polvani 2010).

The SSW associated effects in the atmosphere are now well recognized to extend beyond the polar stratosphere and significant changes have also been witnessed in the mesosphere-lower thermosphere (MLT) and ionosphere regions (e.g., Pedatella et al. 2018). The warming of the winter polar stratosphere during SSWs is associated with the cooling of the winter polar mesosphere (e.g., Labitzke 1972). This mesospheric cooling happens due to the deceleration and potential reversal of the eastward stratospheric ZMW during SSWs, which result in an increased eastward forcing due to gravity waves in the polar mesosphere that induces an upwelling and leads to adiabatic cooling at mesospheric altitudes (e.g., Holton 1983; Liu and Roble 2002; Zülicke and Becker 2013). The changes in gravity wave forcing in the mesosphere also modify the stratosphere-mesosphere residual circulation, which causes warming in the summer hemisphere mesosphere and a decrease in the occurrence of polar mesospheric clouds through inter-hemispheric coupling mechanisms (e.g., Karlsson et al. 2009; Kőrnic and Becker 2010). SSW related effects are also found in the lower thermosphere in the form of warming at polar and mid-latitudes (e.g., Goncharenko and Zhang 2008; Funke et al. 2010; Liu and Roble 2002) but the exact reasons behind this observation is yet to be fully ascertained.

Atmospheric tides have been found to play a key role in coupling the SSW effects to the upper atmosphere (e.g., Chau et al. 2009; Fejer et al. 2010; Goncharenko et al. 2010). Tides in the atmosphere are referred to as planetary-scale oscillations that have periods and sub-periods of a solar (24 h) or a lunar (24.84 h) day. Atmospheric solar tides form the primary components of tidal oscillations and are mainly thermally generated through the absorption of solar radiation by tropospheric water vapour and stratospheric ozone (e.g., Lindzen and Chapman 1969). In contrast, the relatively smaller atmospheric lunar tides are generated due to the gravitational interaction of the moon-Earth system (e.g., Sabine 1847). Tides that are sun- or moon-synchronous are termed as 'migrating' solar or lunar tides. Alternatively, tides that do not follow the motion of the moon or the sun are termed as 'nonmigrating'. In literature, the shorthand notation xWs or xEs are used to denote a westward or eastward propagating tide, respectively, for which s is the zonal wavenumber. For diurnal, semidiurnal and terdiurnal oscillations, 'D', 'S' and 'T' replace 'x' and migrating diurnal, semidiurnal and terdiurnal tides are represented by DW1, SW2 and TW3, respectively.

During SSWs, it has been found that changes in the migrating semidiurnal solar (SW2) and lunar (M2) tides

play an important role in the variability of MLT and ionosphere (e.g., Chau et al. 2012, and references therein). The SW2 enhancements during the SSWs are due to a combination of different factors, which arise due to SSW associated changes in stratosphere-mesosphere chemistry and ZMW. These factors include changes in tidal propagation conditions (e.g., Jin et al. 2012), changes in stratospheric ozone distribution (e.g., Goncharenko et al. 2012; Siddiqui et al. 2019) and non-linear interaction with stationary planetary waves (e.g., Liu et al. 2010). The M2 enhancement is attributed to background zonal mean zonal wind changes, which shifts the secondary (Pekeris) resonance peak of the atmosphere towards the period of M2 tide (Forbes and Zhang 2012).

In addition to the variability in SW2 and M2 tides, SSW-driven changes can also be witnessed in a range of other migrating and nonmigrating tides. Along with the variability in DW1 and TW3 tides, the nonmigrating solar diurnal westward wave-2 (DW2), diurnal stationary (D0), semidiurnal westward wave-1 (SW1) and semidiurnal westward wave-3 (SW3) have been reported to show a strong response to SSW at MLT and ionospheric altitudes (e.g., Jin et al. 2012; Pedatella and Liu 2013; Lin et al. 2013; Lieberman et al. 2015; Sridharan 2017). These responses vary individually for the migrating and nonmigrating tides with differing level of changes seen during SSWs in each one of them. While the DW1 tide at MLT altitudes has been found to show a reduction at low-latitudes during the 2009 SSW from both Sounding of the Atmosphere using Broadband Emission Radiometry (SABER) temperature observations and coupled whole atmosphere model simulations (e.g., Jin et al. 2012; Pedatella et al. 2012; Sassi et al. 2013), the TW3 tide from SABER temperature observations has been found to enhance at low-to-mid-latitudes in the MLT region during the 2009 SSW (Jin et al. 2012). The TW3 enhancement at lower thermospheric altitudes had earlier been posited by Fuller-Rowell et al. (2010) in a simulation based study of the 2009 SSW. Besides the variability of solar diurnal and terdiurnal migrating tides, the variability of higher-order solar migrating tides at MLT altitudes have also been reported during SSWs (e.g., Gong et al. 2018, He et al. 2020). Using a network of mid-latitude specular meteor radars, He et al. (2020) found that the amplitudes of fourth (6 h), fifth (4.8 h) and sixth (4 h) harmonics of migrating solar tide quench after the SSW onset.

Although the SSW associated changes in migrating and nonmigrating tides have been well documented, the key mechanisms behind their variability, barring the SW2 and M2 tides, have not been thoroughly investigated. While earlier works such as by Sassi et al. (2013) have focused on the DW1 tidal variability during the 2009 NH

SSW, there have been no further reports investigating the DW1 tidal variability during other NH SSWs or any SH SSWs in great detail. The objective of this study is to examine and understand the variability of the DW1 tide in the MLT region during multiple NH and SH SSWs. For this purpose, we use SABER temperature observations and reanalysis-driven Whole Atmosphere Community Climate Model with thermosphere and ionosphere extension (WACCM-X) simulations. The evolution of the DW1 tide is investigated during four NH SSWs and two SH SSWs in this study. For the NH SSWs, we select the 2006, 2009, 2010 and 2013 warming events and for the SH SSWs, we choose the 2002 and 2019 warming events in our analysis. The NH SSWs have been chosen in a way so as to include major SSWs that have occurred under varying solar flux conditions. The 2009 and 2010 NH SSWs took place under low solar flux levels while the 2006 and 2013 NH SSWs were realized under moderate-to-high solar flux conditions. By selecting these four events, we explore whether the MLT DW1 tide shows any discernible variability with varying solar flux levels during SSWs since it is known that the MLT DW1 tide shows higher amplitudes during low solar flux periods and lower amplitudes during high solar flux periods (e.g., Sridharan et al. 2010, Singh and Gurubaran 2017). In a similar manner, we select the 2002 and 2019 SH SSWs for our analysis since these two events are among the strongest SSWs that have ever happened in the SH with the 2002 and 2019 SH SSWs occurring under high and low solar flux conditions, respectively. In addition, we investigate whether the changes in the latitudinal shear of MLT zonal winds at low-latitudes, which are known to strongly affect the seasonal variation of the DW1 tide, could explain the observed variability of the DW1 tide during NH and SH SSWs. The structure of this paper is as follows. In "Data and methods" section, the data and methods used in this study are provided. The results are presented in "Results" section, which is followed by discussion in "Discussion" section. The conclusions from this work are presented towards the end.

Data and methods

MLT DW1 tide from SABER temperature measurements

The Sounding of the Atmosphere using Broadband Emission Radiometry (SABER) instrument onboard the National Aeronautics and Space Administration (NASA) Thermosphere Ionosphere Mesosphere Energetics and Dynamics (TIMED) satellite performs global measurements of the atmosphere by using a 10-channel broadband limb-scanning infrared radiometer, which covers the spectral range between 1.27 and 17 μm . The SABER limb scans use infrared CO_2 emissions at 4.3 and 15 μm to derive temperature profiles between 20–120 km

(Remsberg et al. 2008). The TIMED satellite precesses in local time at a rate of ~ 12 min/day and it covers a full 24-h cycle of local time in 60 days (e.g., Zhu et al. 2005). Tidal decomposition of SABER temperature data using standard spectral Fourier diagnostics or least-squares fitting approach therefore requires 60 days of combined ascending (asc) and descending (dsc) orbit nodes observations (e.g., Forbes et al. 2008; Pancheva and Mukhtarov 2011). The tidal amplitude that is obtained using this method represents an average over the 60 days period and is insufficient to capture tidal variability on shorter timescales (e.g., Lieberman et al. 2015; Pedatella et al. 2016). In case of diurnal tides, however, short-term variability can be inferred from an alternative mathematical approach commonly referred to as 'tidal deconvolution'. This method does not require complete 24-h local time sampling of satellite data and has been utilized in earlier studies to investigate the short-term variability of various diurnal tides from SABER temperature data (e.g., Oberheide et al. 2003; Lieberman et al. 2015, Vitharana et al. 2019, Kumari and Oberheide 2020).

The tidal deconvolution method relies on the differencing between the daily measurements taken on the asc and dsc portions of the satellite orbit and can be applied at those latitudes where the local solar time difference between the asc/dsc orbit nodes is ideally ~ 12 h. With the use of such differencing, the semidiurnal tidal components and low-frequency planetary-scale waves vanish in the asc-dsc difference fields (e.g., Oberheide et al. 2002, 2003). From the perspective of a quasi-Sun synchronous satellite, a diurnal tide with a zonal wavenumber s is viewed as one with a zonal wavenumber $s - 1$ in case of westward propagation and as one with a zonal wavenumber $s + 1$ in case of eastward propagation (Salby 1982). The amplitude of the DW1 tide is estimated from the vertical structure of the zonal mean component of the SABER asc-dsc difference fields as the DW1 tide is aliased to the zonal mean ($s = 0$) from the satellite perspective (e.g., Lieberman 1991; Oberheide et al. 2000; Lieberman et al. 2015).

We apply this tidal deconvolution method to SABER observations to retrieve daily amplitudes of DW1 tide and present results based on a running 10-day average of the daily values. This averaging reduces the impact of spurious observations and occasionally large day-to-day variability in the estimated DW1 tide. The uncertainty in DW1 tidal amplitudes estimated by tidal deconvolution is < 1 K (Lieberman et al. 2015), which arises partly because the SABER asc and dsc nodes are separated by ~ 9 h in local time. When the asc-dsc difference fields are not separated by 12 h in local solar time then there is a potential for aliasing by semidiurnal tides. However, aliasing by semidiurnal tides has been found to be within the error

limits at latitudes equatorward of 30° and at altitudes below 90 km (e.g., Vitharana et al. 2019). For a more detailed overview of the tidal deconvolution method, the readers can refer to Oberheide et al. (2002).

MLT DW1 tide from WACCM-X simulations

We employ the Whole Atmosphere Community Climate Model with thermosphere and ionosphere extension (WACCM-X version 2.1) (Liu et al. 2018) to perform the model simulations in this study. WACCM-X is the atmospheric component of the National Center for Atmospheric Research (NCAR) Community Earth System Model (CESM) (Hurrell et al. 2013) that extends from the surface to the upper thermosphere, with a model top boundary, depending on solar activity lying between 500 and 700 km. As WACCM-X is built upon the regular WACCM (version 4) (e.g., Marsh et al. 2013), it incorporates all the physical processes represented in WACCM4 up to the lower thermosphere. The horizontal spatial resolution of WACCM-X is 1.9° in latitude and 2.5° in longitude. In the vertical direction, WACCM-X uses a hybrid σ - p coordinate system, which is purely pressure based above 100 hPa. The vertical resolution for WACCM-X in $\log(p)$ coordinates varies from ~ 0.16 in the troposphere and lower stratosphere

to 0.25 in the mesosphere and thermosphere (see Fig. 1, Pedatella et al. 2019). The implementation of a coupled ionosphere with self-consistent ionospheric electrodynamics in WACCM-X is primarily based on the Thermosphere-Ionosphere-Electrodynamics General Circulation Model (e.g., Richmond et al. 1992; Qian et al. 2014). A more detailed description about the new developments incorporated in WACCM-X can be found in Liu et al. (2018). The ‘specified dynamics (SD)’ configuration of WACCM-X, commonly referred to as SD-WACCM-X, can be used to reproduce the atmospheric state during specific time periods by constraining the model toward meteorological reanalysis products. In the present study, we use the SD-WACCM-X configuration to relax the tropospheric and stratospheric dynamical fields (nudging up to ~ 1 hPa) in the model toward NASA Modern Era Retrospective Analysis for Research and Applications (MERRA) version 2 (Gelaro et al. 2017).

Hourly outputs of neutral temperature from SD-WACCM-X simulations are used to extract the amplitude of the DW1 tide at MLT altitudes. At a particular geographic location, solar tidal oscillations can be represented in the following form:

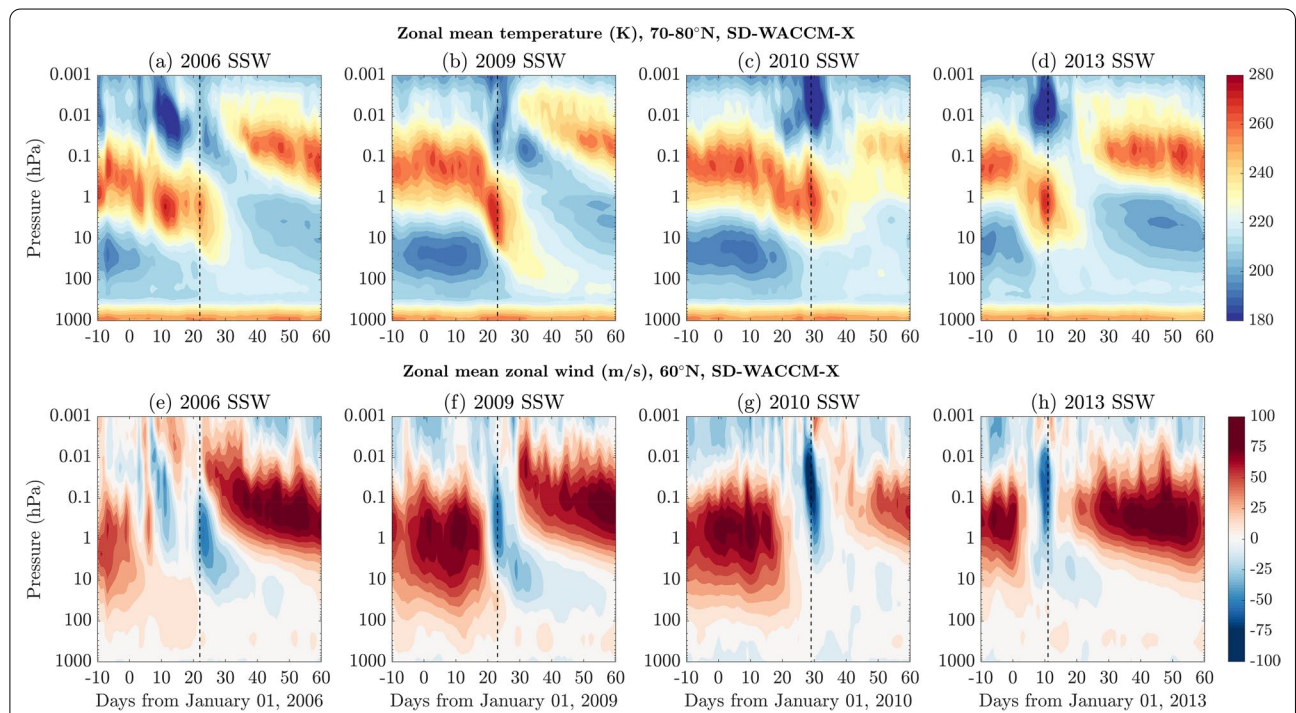


Fig. 1 The top panels present the daily zonal-mean temperature (K) averaged between 70°N and 80°N as a function of pressure levels from SD-WACCM-X simulations for (a) 2006, (b) 2009, (c) 2010 and (d) 2013 NH SSWs. The bottom panels present the SD-WACCM-X simulated daily zonal-mean zonal winds (m/s) at 60°N as a function of pressure levels for the above-mentioned SSWs in e–h. The black dashed lines mark the day of polar vortex weakening (PVW) for the corresponding SSWs

$$\sum_{s=-5}^{s=5} \sum_{n=0}^3 A_{n,s}(\theta, h) \cos(n\Omega t + s\lambda - \phi_{n,s}(\theta, h)) \quad (1)$$

where $\Omega = \frac{2\pi}{24h}$, t is universal time (UT) in hours, n denotes the harmonics and subharmonics of a solar day, s is the zonal wave number, λ is the longitude. $A_{n,s}$ and $\phi_{n,s}$ represent the amplitude and phase of respective tidal components at latitude (θ) and altitude (h), respectively. The tidal phase, $\phi_{n,s}$, is calculated with respect to 0° longitude. For a westward propagating wave, $s > 0$, while $s < 0$ for an eastward propagating wave. We estimate daily amplitudes of the DW1 tide in SD-WACCM-X simulated neutral temperature by performing a least-squares fit to equation 1 with a sliding window of 10 days at each latitude. The 10-days sliding window is chosen for consistent comparison with the SABER DW1 tides. We present the DW1 tides that are estimated from SD-WACCM-X simulations and SABER temperature observations during the NH and SH SSWs in the following sections.

Results

Zonal-mean variability

NH SSWs

Figure 1 presents an overview of dynamical conditions of the Arctic polar atmosphere using the temperature and wind outputs from SD-WACCM-X simulations during the 2006, 2009, 2010 and 2013 major NH SSWs. The top panels in Fig. 1 present the pressure-time plots of the zonal-mean temperature averaged between 70 and 80°N for all these four major warming events (Fig. 1a–d). The black dashed lines in the figure mark the day of polar vortex weakening (PVW), which is a definition used for identifying the peak phase of SSW. As an alternative to the classical SSW definition, PVW has been used in recent studies to correlate the tidal enhancements in the MLT and ionosphere with the magnitude of the reversal of stratospheric zonal-mean zonal wind (e.g., Zhang and Forbes 2014; Chau et al. 2015; Siddiqui et al. 2015). The list of SSWs and their respective PVW dates are indicated in Table 1.

The evolution of the stratopause during these SSWs bears a resemblance to each other with the most notable common feature being the rapid descent of the stratopause from its climatological position (~ 0.1 hPa) during the SSW onset. The descent of the stratopause begins around day -5 for the 2006 SSW, day 18 for the 2009 SSW, day 15 for the 2010 SSW and day 0 for the 2013 SSW. Among these four SSWs, the stratopause is seen to drop deepest during the 2009 SSW and the least during the 2010 SSW. During these four major SSWs, the stratopause descent is accompanied by its warming and followed by its breakdown and reemergence at a higher altitude. The rapid drop in the stratopause

Table 1 List of NH and SH SSWs (year of occurrence) and their respective PVW (dd/mm) dates

SSWs	Hemisphere	PVW dates
2002	SH	26/09
2006	NH	22/01
2009	NH	23/01
2010	NH	29/01
2013	NH	11/01
2019	SH	19/09

altitude leads to warming in lower altitudes, which happens before the stratopause breaks down in the peak phase of the SSWs (black dashed lines). Around this same time, another common feature seen in all four SSWs is cooling above 0.1 hPa in the mesosphere, which is known to accompany warming in the stratosphere (e.g., Zülicke et al. 2018). The breakdown in stratopause results in the formation of a nearly isothermal stratosphere as seen around day 30 for the 2006 SSW, day 35 for the 2009 SSW, day 40 for the 2010 SSW and day 20 for the 2013 SSW. Later, the stratopause is seen to reform with cooler temperatures and reappear as a well-defined structure in the recovery phase of each of the SSWs at an elevated altitude near 0.01 hPa (e.g., Siskind et al. 2007; Manney et al. 2009). The reformation of the stratopause at a higher altitude is referred to as elevated stratopause event and is attributed to mesospheric PW activity and non-orographic gravity wave (GW) drag after the SSWs (e.g., Chandran et al. 2011; Limpasuvan et al. 2012).

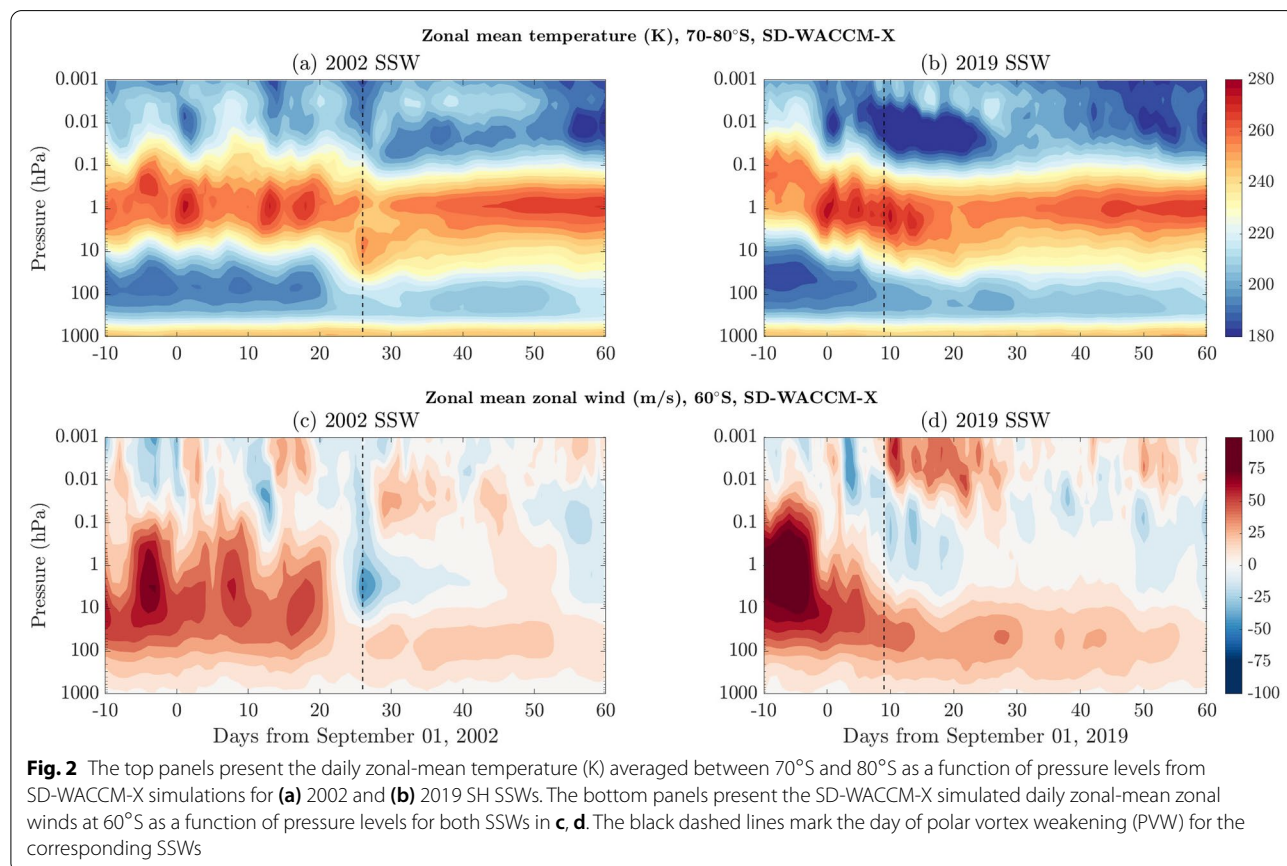
The bottom panels in Fig. 1 (Fig. 1e–h) present the daily zonal-mean zonal winds at 60°N as a function of pressure levels from SD-WACCM-X simulations of the above-mentioned SSWs. Like zonal-mean temperature, we also observe a common feature in zonal-mean zonal winds during these SSWs, which happens to be the early appearance of westward ZMZW in the mesosphere that later descends through the stratosphere and eventually reaches the upper troposphere. The mesospheric wind reversals precede those in the stratosphere and are associated with the filtering of upward propagating GWs during SSWs (e.g., Hoffmann et al. 2002, 2007). The SSW-associated disturbance in stratospheric zonal winds changes the filtering conditions for upward propagating GWs, which results in only eastward propagating GWs reaching up to the mesosphere. As a result of this change in mesospheric forcing due to altered GW fluxes, a net eastward GW anomaly is introduced, which leads to upwelling and cooling in the polar mesosphere (e.g., Holton 1983).

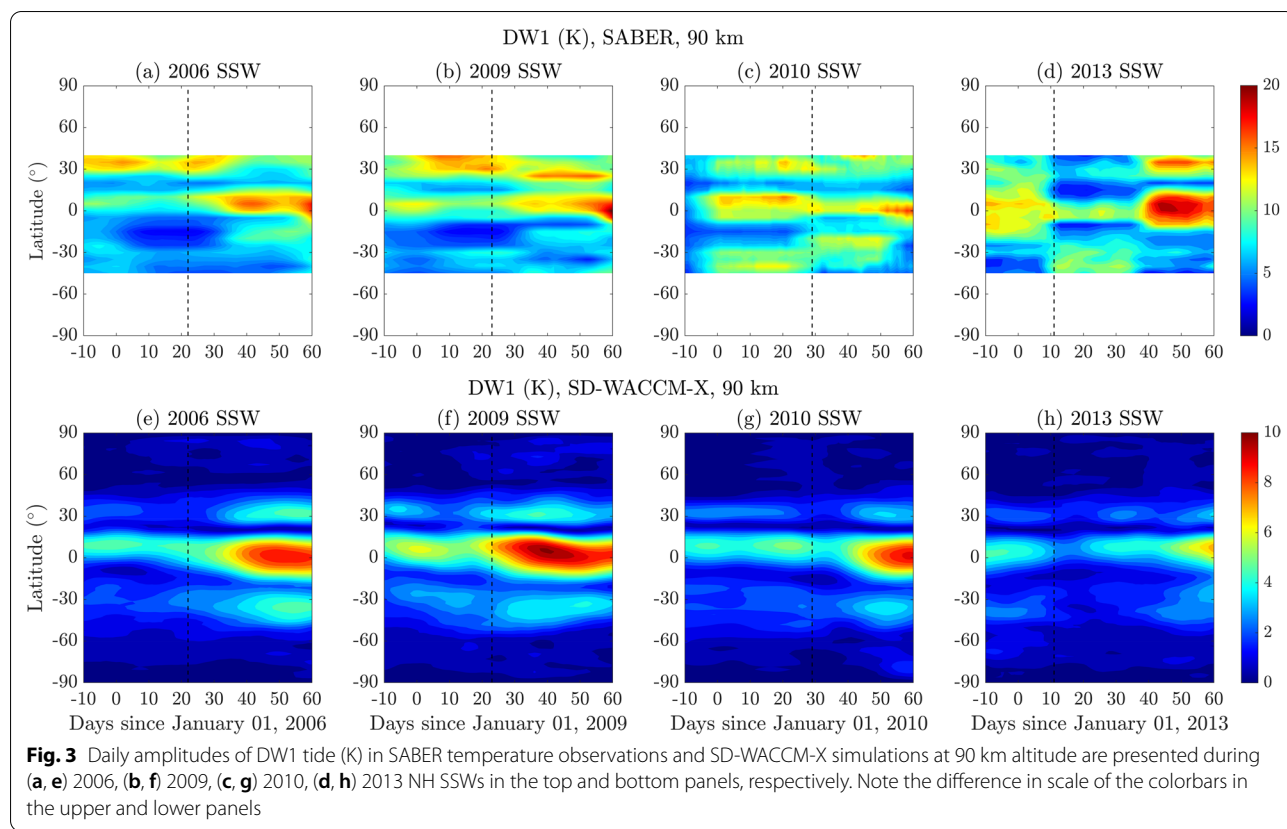
From Fig. 1, we note that SD-WACCM-X simulations reproduce the temperature and wind structures of the SSWs in a consistent manner. The SD-WACCM-X simulated zonal-mean temperatures have been compared with Aura Microwave Limb Sounder (MLS) and SABER temperature observations during SSWs in earlier studies (e.g., Pedatella et al. 2014a, b) and a good agreement between observations and simulations have already been reported. A comparison between the simulated and observed zonal-mean temperatures have therefore not been presented in this study.

SH SSWs

Figure 2 gives an overview of dynamics of the Antarctic polar atmosphere during the 2002 and 2019 SH SSWs through the vertical time sections of the simulated zonal mean temperature averaged between 70 and 80°S and zonal-mean zonal winds at 60°S. The black dashed lines mark the days of PVW during the respective SSWs. In Fig. 2a, the descent of the stratopause during the 2002 SSW can be witnessed as it drops from a mean altitude of ~48 km (1 hPa) around day 20 to ~32 km (10 hPa) around day 26, which leads to warming in the lower stratosphere. Around this same period, the cooling of the mesosphere

can also be seen above 0.1 hPa. From Fig. 2c, we notice that the westward ZMZW begin appearing in the mesosphere (above 0.1 hPa) since the beginning of September but the reversal of the mesospheric ZMZW remains transient and does not descend into the stratosphere until around day 22. Thereafter, the westward ZMZW descend from the mesosphere and eventually reach below 10 hPa level by day 24. In case of the 2019 SSW event, we see the descent and warming of stratopause between days 0 and 20 in Fig. 2b. The intensity of warming in the lower stratosphere (~10 hPa) is found to be stronger for this event in comparison to the 2002 SSW, which was also confirmed in an earlier study by Yamazaki et al. (2020). It is to be noted that unlike the four NH SSWs that we have studied, there is no development of elevated stratopause during the 2002 and 2019 SH SSWs. The readers may also note that not all SSWs in the NH display development of elevated stratopause. From Fig. 2d, the appearance of westward ZMZW in the mesosphere is seen around day 2 and it subsequently descends a week later into the stratosphere. Unlike the 2002 SSW, the westward ZMZW during the 2019 SSW do not reach down to the 10 hPa level so this event is classified as a minor warming.





MLT DW1 tidal variability NH SSWs

Figure 3 shows the temporal evolution of DW1 tidal amplitude obtained from SABER temperature observations (upper panels) and SD-WACCM-X simulations (lower panels) at 90 km altitude during the 2006, 2009, 2010 and 2013 NH SSWs. The black dashed lines mark the corresponding PVW days for each SSW event. For all four periods shown in Fig. 3, the DW1 tide exhibits its well-known features with largest amplitude in temperature at low-latitudes along with an enhancement in its amplitude towards the end of February, which is part of its semi-annual variation in the MLT (e.g., Hays and Wu 1994; Vincent et al. 1998; Gan et al. 2014). We note that simulations are able to reproduce these aspects of temporal evolution of DW1 tide with great consistency for all the shown SSW periods but with reduced amplitudes. The underestimation of DW1 amplitude in WACCM-X simulations in the MLT as compared to that of in SABER temperature observations has been reported in many studies (e.g., Lu et al. 2012; Liu et al. 2018, 2021). The underestimation of simulated DW1 probably results due to an underestimation of the diurnal cycle in parameterized convection processes in WACCM-X (Lu et al. 2012). In Fig. 3, the DW1 tidal amplitudes also

show a pronounced minimum associated with SSWs at low-latitudes, which is clearly seen in observations and reproduced in simulations. For the 2006 SSW event, the decline in DW1 can be seen between days 10 and 20 in the latitude range 0–15°N in Fig. 3a. The DW1 tidal amplitude declines from a peak of ~11 K around day 0 to a minimum of ~9.5 K by day 14 before enhancing back to a maximum of ~16 K by day 40 in Fig. 3a. The simulated DW1 tide for the 2006 SSW shows similar characteristics in Fig. 3e as in Fig. 3a with a decline of ~1 K between 0 and 10°N around day 10 and an enhancement beginning around day 30 following the peak of the SSW. During the 2009 SSW event, the DW1 tidal amplitude in Fig. 3b shows similar features as during the 2006 SSW with a marked decline around day 10 just prior to the SSW peak that lies between periods of DW1 enhancements. The DW1 amplitude declines from a peak value of ~13 K around day 0 between 0–10°N to ~11 K around day 13 before enhancing back to ~13 K levels by day 30. The simulated DW1 tide in Fig. 3f captures this observed DW1 tidal behavior in Fig. 3b with a decline of ~1 K also seen around day 10 in the 0–10°N latitude band in comparison to its peak value of ~6 K around day 0. Following the SSW peak, the DW1 tidal amplitude in Fig. 3f enhances and reaches up to ~10 K levels around day 40.

For the 2010 and 2013 SSWs as well, we witness similar DW1 tidal weakening around the PVW days in Figs. 3c and 3d, respectively. For these two events, the DW1 tide also shows enhancement prior to and after the SSW peaks at low-latitudes. In case of 2010 SSW, the decline in DW1 tidal amplitude of ~ 2 K is seen at low-latitudes between days 30 and 40 in Fig. 3c, whereas in case of 2013 SSW, the decline in DW1 amplitude of ~ 3 K is recorded after the PVW day. The simulated DW1 tidal amplitudes in Fig. 3g and 3h reproduce the observed variability in DW1 tides during the 2010 and 2013 SSWs to a good extent and we notice a decline of ~ 1 K and ~ 2 K, respectively, in simulated DW1 tide during both these SSWs. The enhancements of DW1 tide prior to the PVW days and towards the end of February during 2010 and 2013 SSWs are also reproduced in simulations in Fig. 3g and h, albeit with lower amplitudes. From Fig. 3, we also find that the DW1 tide during these four SSWs displays similar amplitudes and any possible influence of solar flux levels is not clearly discernible.

SH SSWs

Figure 4 presents the temporal variability of DW1 tide at 90 km altitude during the 2002 and 2019 SH SSWs from SABER temperature observations (upper panels) and

SD-WACCM-X simulations (lower panels). The black dashed lines mark the PVW days for both SSWs. For both these SH SSWs, the latitude-time structure of DW1 in SABER and SD-WACCM-X are found to be consistent with each other especially at low-latitudes. However, the amplitude of DW1 at the shown altitude is relatively lower ($\sim 50\%$) in simulations as compared to observations and the plausible reason for this underestimation of DW1 in SD-WACCM-X simulations has been discussed earlier in Section 2.1. For the 2002 SSW, the DW1 tide in SABER observations (Fig. 4a) is found to show enhancement centered around day 10 with peak amplitude reaching ~ 13 K between 20° S and 5° N followed by a weakening of ~ 2 K just prior to SSW onset between days 15 and 20. The DW1 tide enhances back to above 13 K levels post day 22 at low-latitudes and continues to gradually increase in October. The simulated DW1 tide for the 2002 SSW in Fig. 4c shows similar variability as in observations with peak enhancement reaching ~ 8 K centered around day 10 at low-latitudes, which is followed by a weakening of ~ 3 K between days 18 and 26 and a further enhancement in the beginning of October. For the 2019 SSW, the evolution of DW1 tide in SABER observations in Fig. 4b shows similar features as during the 2002 SSW with a prominent weakening in amplitude at low-latitudes close

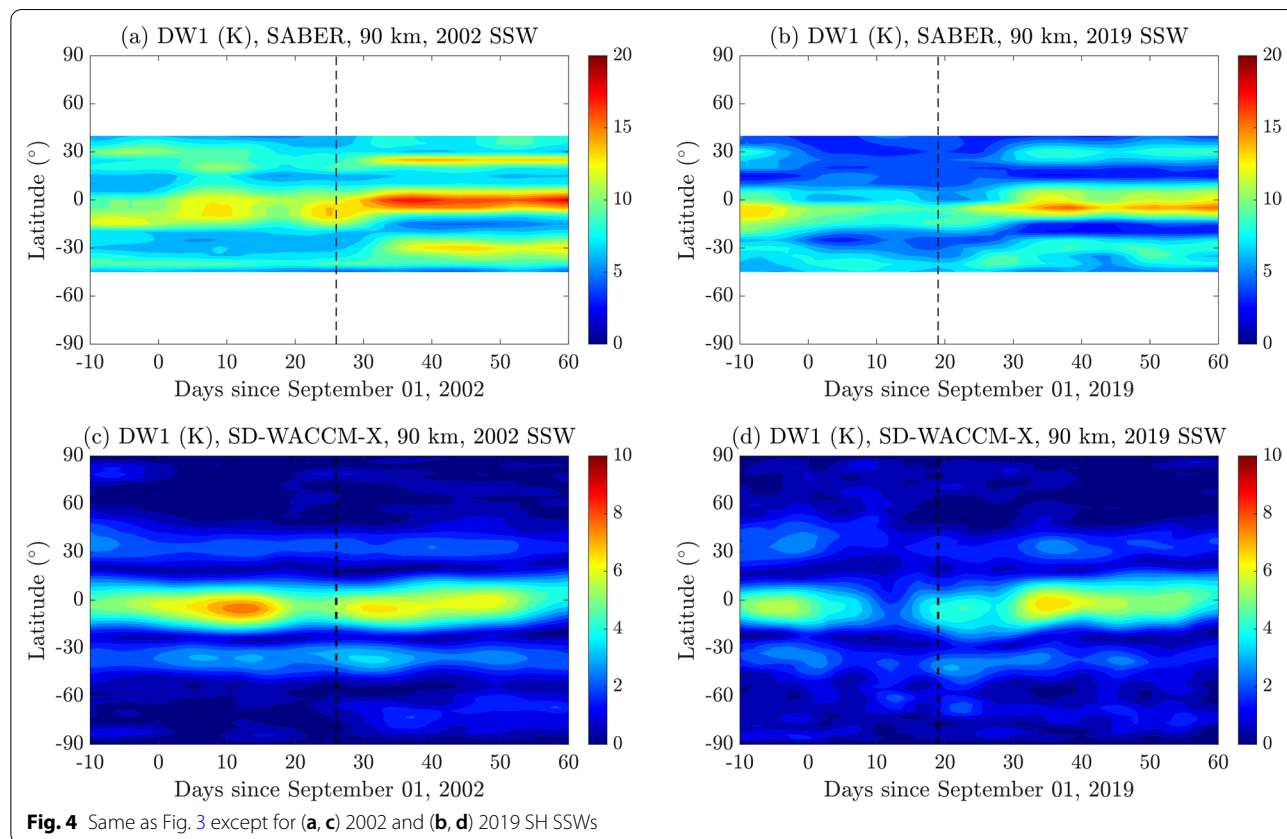


Fig. 4 Same as Fig. 3 except for (a, c) 2002 and (b, d) 2019 SH SSWs

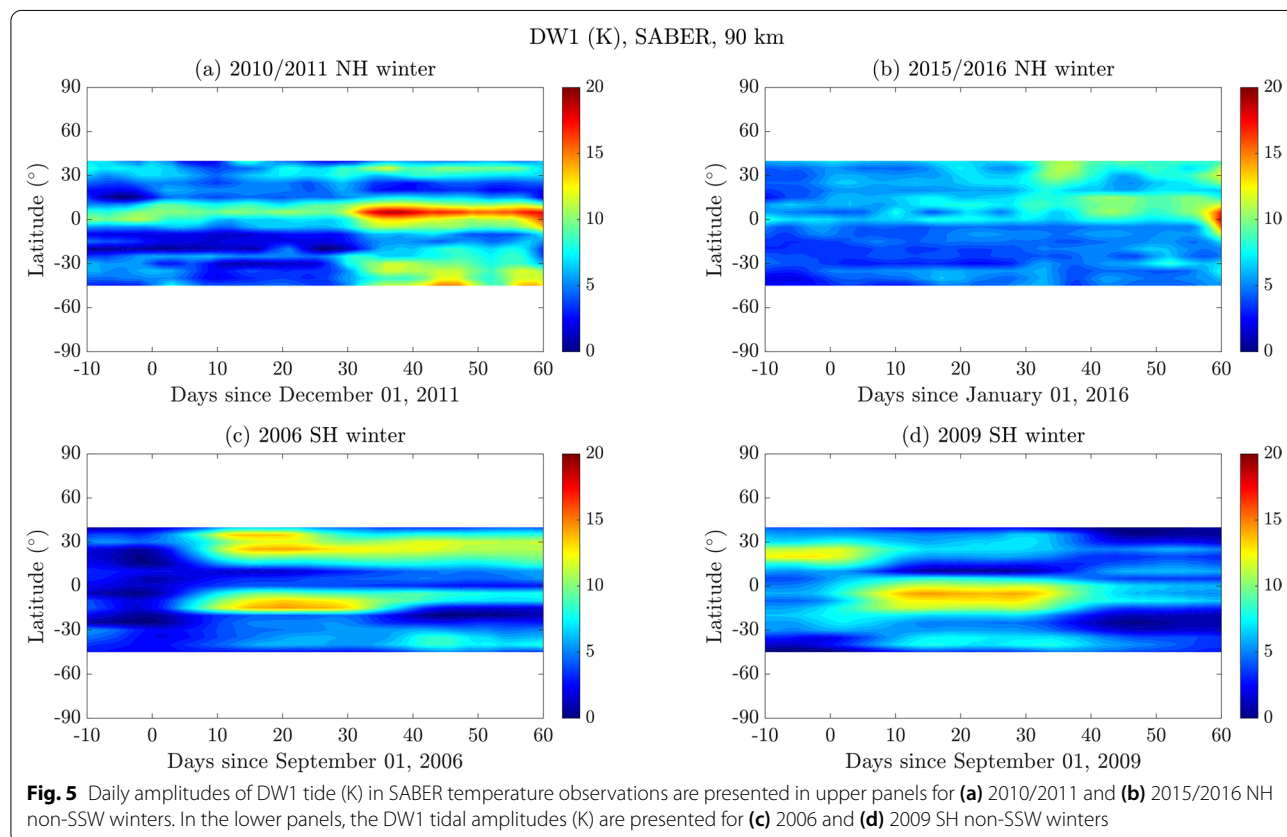
to the PVW day. In Fig. 4b, the DW1 amplitude declines from a peak amplitude of ~ 14 K between 0 and 20°S around day -10 to ~ 9 K between days 10 and 20 and later gradually enhances at the beginning of October. For the 2019 SSW, the simulated DW1 tide in Fig. 4d reproduces the observed variability in Fig. 4b. A notable decline centered around day 10 is seen in the DW1 tide in Fig. 4d. The DW1 tidal amplitude in this figure declines from ~ 6 K around day -5 to ~ 3 K around day 10 before enhancing back to above ~ 6 K levels in October.

From Figs. 3 and 4, we can note that the evolution of DW1 tide during NH and SH SSWs resemble each other, which is marked by a decline of DW1 tide around the PVW days. In the next section, we discuss the mechanism that could be responsible for this variability of DW1 tide during both NH and SH SSWs.

DW1 tidal variability during non-SSW NH & SH winters

The DW1 tidal variability during NH and SH SSWs were shown in Figs. 3 and 4, respectively. As a reference, we present the temporal evolution of DW1 tidal amplitudes during NH and SH non-SSW winters in Fig. 5. We select the 2010/2011 and 2015/2016 NH winters as both these periods were associated with strong stratospheric Arctic polar vortex and low PW activity (e.g., Hurwitz et al.

2011; Matthias et al. 2016). Similarly for SH winters, we choose the period between August and October in 2006 and 2009, as the Antarctic polar vortex was found to remain notably strong in these years (e.g., Zuev and Saveleva 2019). The DW1 tidal amplitude from SABER temperature observations during 2010/2011 and 2015/2016 NH winters are shown in upper panels in Fig. 5a and b, respectively. For both these periods, we notice that the DW1 tide has larger amplitudes at low-latitudes in February than in January, which is consistent with its seasonal variations. In Fig. 5a, the DW1 amplitude during the 2010/2011 NH winter remains around 12 K between 10°N – 10°S in January and enhances to ~ 20 K in February. During the 2015/2016 NH winter, the DW1 amplitude at low-latitudes in Fig. 5b enhances from ~ 7 K in January to ~ 10 K by mid-February and to ~ 20 K towards the end of February. Unlike the DW1 tidal variability during NH SSWs in Fig. 3, we find no evidence of sharp decline in DW1 amplitudes at low-latitudes during both 2010/2011 and 2015/2016 NH winters. In the lower panels, the DW1 tidal amplitude from SABER temperature observations during 2006 and 2009 SH winters are shown in Fig. 5c and d, respectively. During both these periods, we find that the DW1 tide at low-latitudes peaks during the month of September with amplitudes reaching ~ 15



K. During these periods as well, we do not find any sharp reduction in the DW1 tidal variability as we observed during the SH SSWs in Fig. 4. On comparing the DW1 tidal variability during non-SSW winters with those during SSW winters, we find that the short-term decline of DW1 tide in the MLT is a common feature associated with both NH and SH SSWs.

Discussion

Following the numerical work of McLandress (2002), it is now known that the DW1 tide at MLT altitudes is sensitive to changes in latitudinal shear of the zonal-mean zonal winds in the MLT region. Due to the large phase speed of the DW1 tide ($c \sim 400$ m/s at the equator), the effect of changes in the zonal-mean zonal winds on the propagation of the DW1 tide seems unlikely. However, DW1 tide has been found to be strongly sensitive to the latitudinal shear in zonal-mean zonal wind in the MLT region and this shear effect is primarily responsible for its well-known semiannual variation, which is characterized by strong equinoctial and weak solstitial amplitudes (e.g., Hays and Wu 1994; Vincent et al. 1998). The latitudinal shear in the zonal-mean zonal winds introduces a zonal-mean vorticity ($\bar{\zeta}$), which at low-latitudes can be large enough to be comparable to the Coriolis parameter (f). It is found that $\bar{\zeta}$ could affect the DW1 tide indirectly by changing the absolute zonal-mean vorticity ($\eta = f + \bar{\zeta}$) of the background atmosphere. This is qualitatively somewhat analogous to an enhancement or reduction of the Earth's rotation rate, which ultimately determines the width of the latitudinal band or waveguide where the DW1 tide vertically propagates. According to the classical tidal theory, the waveguide for the DW1 tide is restricted near the equator and extends from 30°N to 30°S (Lindzen and Chapman 1969). Positive values of $\bar{\zeta}$ at some altitude result in a faster rotation rate ($\eta > f$), which narrows the waveguide for the vertically propagating DW1 tide while negative values of $\bar{\zeta}$ imply a slower rotation rate ($\eta < f$), which will result in broadening of this waveguide. This in turn will lead to reduction of DW1 tidal amplitude above this altitude in case of the former and an enhancement of DW1 tidal amplitude in case of the latter. Using a numerical model, McLandress (2002) applied this theory to show that the seasonal variation of latitudinal shear in the westward mesospheric ZMW in the subtropics explains the observed semiannual variation of DW1 in the MLT. We suspect that this mechanism, which explains the variability of DW1 tide on seasonal time scales could also be used to explain the variability of DW1 tide on subseasonal time scales during NH and SH SSWs.

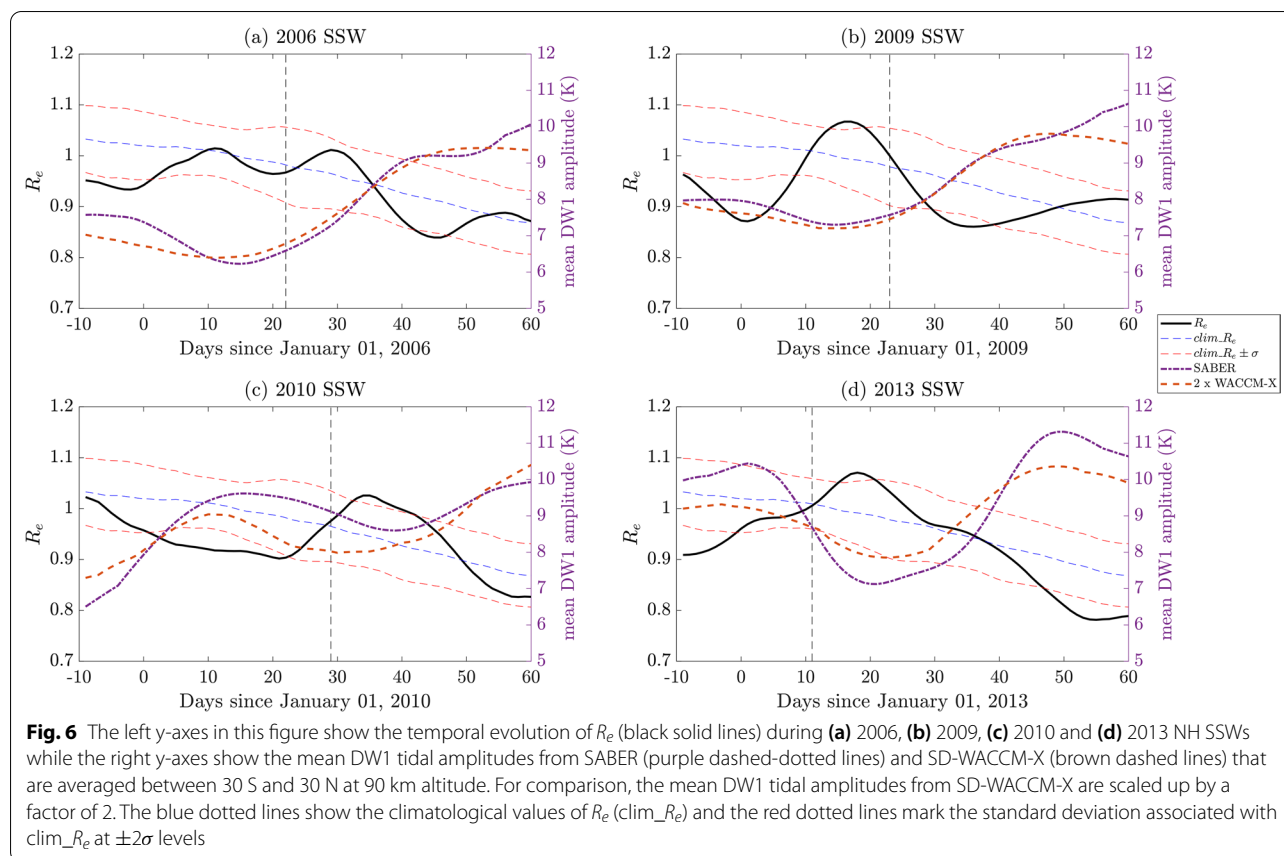
We calculate the ratio of absolute (η) and planetary vorticity (f) and define it as follows:

$$R = \frac{\eta}{f} = \frac{f + \bar{\zeta}}{f} = \frac{f - \bar{u}_y}{f} \quad (2)$$

where, $f = 2\Omega \sin(\phi)$, Ω is the Earth's rotation rate and ϕ is the latitude in degrees. On calculating and neglecting the zonal gradient, the zonal-mean vorticity ($\bar{\zeta}$) simplifies to \bar{u}_y , which is the meridional gradient (y-direction) of the zonal-mean zonal wind (u).

In the NH, a negative meridional shear ($\bar{u}_y < 0$) will increase R , which will lead to narrowing of the waveguide and reduced DW1 amplitudes while a positive meridional shear ($\bar{u}_y > 0$) will reduce R , thus leading to broadening of the waveguide and enhanced DW1 amplitudes in the MLT. Numerical results of McLandress (2002) showed that R varies with maximum values near the solstices ($R \sim 1.5 - 2$) to minimum values near the equinoxes ($R \sim 0.6 - 0.8$). We calculate daily mean values of vorticity ratio, R , between $30^\circ\text{S} - 30^\circ\text{N}$ (excluding the equator), which is then further averaged between 70 and 90 km altitude to obtain an effective R , which is henceforth referred to as R_e . This approach is similar to the one used by Sassi et al. (2013) to explain the DW1 tidal variability during the 2009 SSW.

In Fig. 6, we present the temporal evolution of R_e and compare it with SABER and SD-WACCM-X mean DW1 tidal amplitudes at 90 km altitude that are averaged between $30^\circ\text{S} - 30^\circ\text{N}$ during the (a) 2006, (b) 2009, (c) 2010 and (d) 2013 NH SSWs. The black solid line shows the R_e for respective SSW intervals while the blue dotted line shows the climatological values of R_e (clim_R), which are obtained from a 20-year long SD-WACCM-X run performed for the period 2001-2020. The standard deviation (σ) associated with clim_R are also plotted in Fig. 6 in red dashed lines at $\pm 2\sigma$ levels. The SABER and SD-WACCM-X mean DW1 tidal amplitudes are plotted on the right y-axes in purple dashed-dotted lines and brown dashed lines, respectively, for each of the SSWs. The SD-WACCM-X mean DW1 tidal amplitudes are scaled up by a factor of 2 for plotting it within the same ordinate limits. For the 2006 SSW, it is seen in Fig. 6a that the R_e values initially lie below the -2σ levels between days -10 and 0 before enhancing and reaching climatological levels by day 10. Later R_e declines slightly just before the peak phase of the 2006 SSW and then increases gradually up to day 30. A sharp decline in R_e is seen after this day, which results in its values again being lower than the -2σ levels between days 40 and 50. Thereafter, R_e increases back to its climatological levels towards the end of February. Between days 0 and 20, the temporal variability of the SABER and SD-WACCM-X mean DW1 tidal amplitudes demonstrate a decline with increase in R_e . After day 30, when R_e begins to decline steadily, the amplitude of both observed and modeled mean DW1 tides respond in an



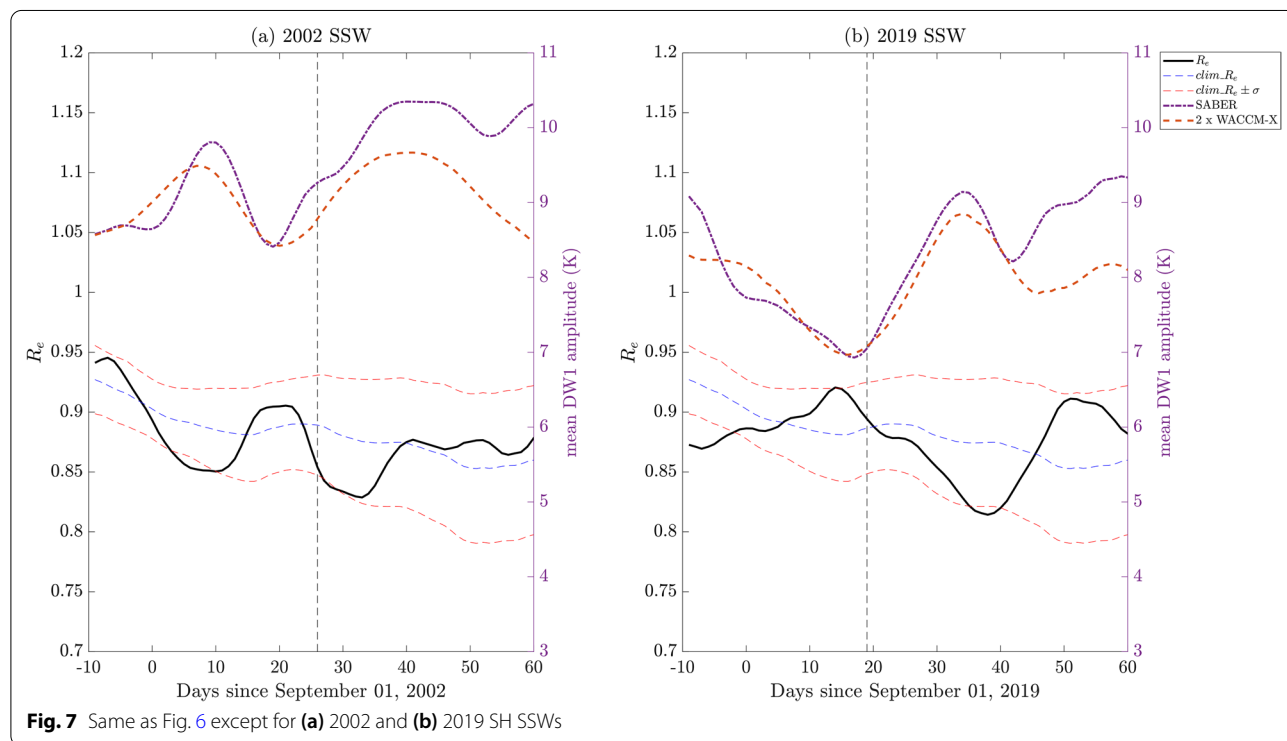
opposite manner and increase during this period. For the 2009 SSW, in Fig. 6b, we see a similar variability in R_e as during the 2006 SSW with R_e values being initially lower than -2σ levels between days -4 and 10 before rising sharply and reaching above the $+2\sigma$ levels around the peak day of the SSW. The R_e values decline sharply again after day 20 and reach below -2σ levels between days 30 and 40 before increasing gradually and reaching back to climatological levels. During the sharp increase in R_e , the SABER and SD-WACCM-X mean DW1 tidal amplitudes reach their minimum between days 10 and 20 before increasing sharply just after the peak SSW phase, which coincide with the decline in R_e . Towards the end of February, the observed and modeled mean DW1 amplitudes follow their seasonal behavior and continue to increase with decreasing R_e . In case of the 2010 SSW, the R_e values in Fig. 6c decline from their climatological levels around day -10 to lower than -2σ levels between days 0 and 20 before sharply increasing during the peak SSW phase to higher than 2σ levels around day 35 . Another steady decline in R_e follows and results in values reaching close to -2σ levels around day 55 . From the SABER and SD-WACCM-X mean DW1 tidal amplitudes, we find an increase between days -10 and 20 that coincide with

the decrease in R_e and a decline between days 21 and 40 , which coincide with the rapid increase in R_e during the peak SSW phase. After day 40 , both observed and modeled mean DW1 tidal amplitudes enhance with the continued decline in R_e . In Fig. 6d, the evolution of R_e during the 2013 SSW is similar in characteristics to the three earlier discussed major NH SSWs. Around day -10 , the R_e values are initially below the -2σ levels but increase steadily thereafter and reach values greater than 2σ levels around day 20 after the peak SSW phase. A sharp decline in R_e ensues after day 20 with its values again declining below the -2σ level around day 50 before recovering subsequently towards the end of February. To a large extent, the evolution of SABER and SD-WACCM-X mean DW1 tidal amplitudes during the 2013 SSW is also opposite to R_e as enhancement in mean DW1 amplitude is seen with declining R_e and a reduction with increase in R_e . As seen during earlier SSWs, the apparent decline in both observed and modeled mean DW1 tidal amplitudes during the 2013 SSW is coinciding with the increase in R_e and its rapid enhancement is coinciding with the decrease in R_e . The readers may note that R_e values during SSWs may reach their peaks earlier (as seen during 2006 and 2009 NH SSW) or later (as seen during

2010 and 2013 NH SSW) than the PVW date since the PVW date is only representative of the peak phase of the SSW and not of the dynamics in the MLT. It is understandable that the SSW-associated changes in the MLT zonal winds and subsequently in R_e may vary in timing with the SSW-associated changes in the stratosphere, which is why we see the decline in DW1 tide to vary with respect to the PVW dates for different SSWs. For all the four NH SSWs, we also find that the variability of SABER and scaled-up SD-WACCM-X mean DW1 tidal amplitudes are consistent with each other.

As in Fig. 6, we present the temporal evolution of R_e in Fig. 7 during the (a) 2002 and (b) 2019 SH SSWs and compare it with the SABER and SD-WACCM-X mean DW1 tidal amplitudes that are averaged between 30°S–30°N at 90 km altitude. The SD-WACCM-X mean DW1 tidal amplitudes presented in this figure are also scaled up by a factor of 2. In Fig. 7, we note that the climatological levels of R_e are lower than in Fig. 6, which is expected as DW1 tides have larger amplitudes near the equinoxes due to lower R_e values as opposed to the solstice periods when the R_e values are comparably larger (e.g., McLandress 2002). In Fig. 7a, the R_e values during the 2002 SSW are seen to decline from above climatological levels around day -10 to below -2σ levels between days 0 and 10, which coincides with the increase in mean DW1 tidal amplitude during this time interval. A return back to climatological levels is witnessed in R_e by day 20, which is

followed by another decline that bottoms out around day 30. During this period, the SABER and SD-WACCM-X mean DW1 tidal amplitudes react in a contrary manner to R_e as their decline coincide with increasing R_e and vice-versa. By day 40, the R_e values decline to climatological levels where they remain till the end of October. During this interval, as R_e follows the declining climatological trend, an increase in the amplitude of SABER and SD-WACCM-X mean DW1 tides can be seen. In Fig. 6b, the R_e values initially lie slightly below -2σ levels around day -10 before steadily increasing to more than 2σ level around day 15. Associated with this increase in R_e , rapid decline in SABER and SD-WACCM-X mean DW1 tidal amplitudes can be seen. Subsequently, R_e levels decline sharply after this day and reach close to -2σ levels around day 35. Both the observed and modeled mean DW1 tidal amplitudes react in an opposite manner to this decline in R_e and increase rapidly. Another episode of increase in R_e is seen beginning around day 40, which coincide with the decline of SABER and SD-WACCM-X mean DW1 tidal amplitudes between days 40 and 50. Towards the end of October, as the R_e values decline back to climatological levels, a gradual increase in both observed and modeled mean DW1 tidal amplitudes is seen during this time interval. From Figs. 6 and 7, we conclude that the temporal evolution of R_e in the upper mesosphere, to a great extent, is opposite to the variability of the DW1 tidal amplitudes during both NH and SH



SSWs. We calculate the Pearson’s correlation coefficients between R_e and SABER and SD-WACCM-X mean DW1 tidal amplitudes shown in Figs. 6 and 7 and present them in Table 2. We note that both the observed and modeled mean DW1 tidal amplitudes demonstrate an anti-correlation with R_e , which is stronger for NH SSWs as compared to SH SSWs. The correlation coefficients between SD-WACCM-X mean DW1 tidal amplitudes and R_e are only slightly higher than between SABER mean DW1 tidal amplitudes and R_e , which suggests that modeling results are consistent with observations and do not differ significantly.

The anti-correlation between DW1 tidal amplitudes and SSW-associated low-latitude changes in MLT zonal-mean vorticity as implied by our results is plausible since there are numerous reports demonstrating significant changes in low-latitude MLT winds during SSWs (e.g., Shepherd et al. 2007; Sathishkumar et al. 2009; Chen et al. 2012). In a case-study of the tropical MLT zonal wind changes during a minor NH SSW in February 1993, Shepherd et al. (2007) reported rapid deceleration and reversal of climatologically eastward zonal winds between 70 and 85 km using medium-frequency (MF) radar measurements from Tirunelveli (8.7°N, 77.8°

E). During this event, the eastward zonal winds reversed to westward by declining from ~ 40 m/s to ~ -5 m/s over a 3 weeks period at around 80 km altitude prior to the onset of February 1993 NH SSW (see Fig. 3, Shepherd et al. 2007). Using the MF radar data at Tirunelveli, Sathishkumar et al. (2009) analyzed the evolution of tropical MLT zonal winds around 80 km altitude during the major NH SSWs in December 1998 and January 2006 and found them to decelerate and reverse from eastward to westward direction during the course of these SSWs (see Fig. 5, Sathishkumar et al. 2009). In the sub-tropics, the deceleration and reversal of MLT zonal winds between 80 and 90 km altitude from eastward to westward direction was also reported by Chen et al. (2012) during the 2001 NH major SSW using radar measurements from Wuhan (30°N, 114°W). They found that at these altitudes, the absolute change in MLT zonal winds could reach up to ~60 m/s as it decelerated and turned westward within a 10 days period during the course of 2001 NH major SSW. These studies indicate that the SSW-associated effects extend far beyond the polar middle atmosphere and substantial changes in MLT zonal winds can even be observed at low-latitudes. It is therefore plausible that SSW-associated changes in MLT zonal winds at low-latitudes lead to changes in zonal-mean vorticity, which result in the enhancement or reduction of DW1 tidal amplitudes. By means of a diagram, we summarize this suggested mechanism in Fig. 8, which helps us to explain the evolution of DW1 tide during NH and SH SSWs.

Table 2 Pearson’s correlation coefficient (r) between R_e and mean DW1 tidal amplitudes from SABER and SD-WACCM-X for the listed NH and SH SSWs

SSWs	R_e & SABER DW1	R_e & SD-WACCM-X DW1
2002 SH	- 0.61	- 0.64
2006 NH	- 0.84	- 0.88
2009 NH	- 0.72	- 0.81
2010 NH	- 0.77	- 0.85
2013 NH	- 0.81	- 0.89
2019 SH	- 0.67	- 0.73

Conclusions

The variability of the MLT DW1 tide during NH and SH SSWs is reported in the present study using SABER temperature observations and SD-WACCM-X simulations. We focused this work on examining the evolution of DW1 tide during four major NH SSWs that occurred in January in 2006, 2009, 2010 and 2013 and two SH SSWs that took place in September in 2002 and 2019. In our analysis, we use a ‘tidal deconvolution’ approach to

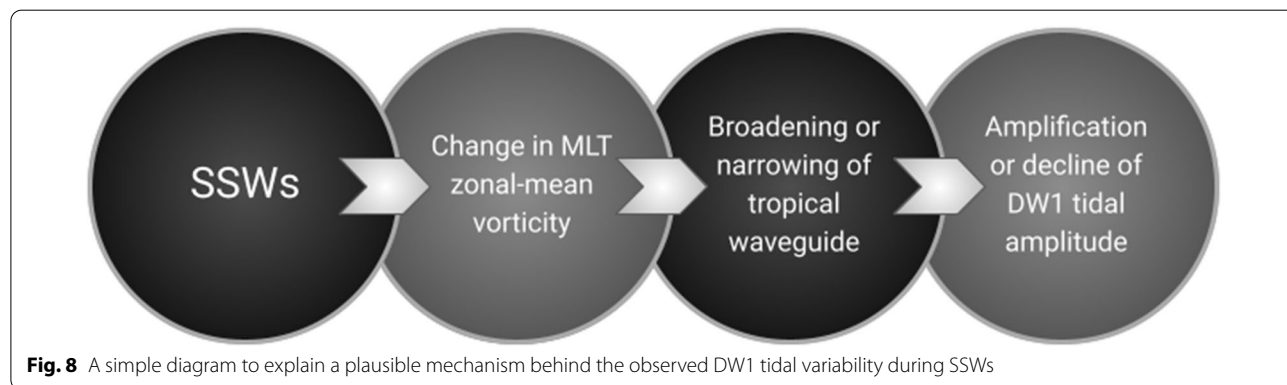


Fig. 8 A simple diagram to explain a plausible mechanism behind the observed DW1 tidal variability during SSWs

estimate the DW1 tide in MLT region from SABER temperature observations. Results show that the observed DW1 tide displays reduced amplitude at low-latitudes after the onset of both NH and SH SSWs. To explain these results, we explore whether the SSW-associated changes at low-latitudes in latitudinal shear of MLT zonal winds, which strongly affects the seasonal variation of MLT DW1 tide, could be a reason for the decline of DW1 amplitudes during both NH and SH SSWs. Using SD-WACCM-X, we find that SSW-associated intraseasonal changes in the latitudinal shear of MLT zonal winds are comparable to the changes that happen on seasonal scales in the latitudinal shear of MLT zonal winds. We suggest that this latitudinal shear mechanism explains the observed decline of DW1 tide that is common to both NH and SH SSWs.

Abbreviations

CEM2: Community Earth System Model; DSO: Nonmigrating Solar Diurnal Stationary; DW1: Migrating Solar Diurnal Tide; DW2: Nonmigrating Solar Diurnal Westward Wave-2; GWs: Gravity Waves; M2: Migrating Lunar Semidiurnal Tide; MERRA: Modern Era Retrospective Analysis for Research and Applications; MLS: Microwave Limb Sounder; MLT: Mesosphere-lower thermosphere; NASA: National Aeronautics and Space Administration; NCAR: National Center for Atmospheric Research; NH: Northern Hemisphere; PVW: Polar Vortex Weakening; PW: Planetary Wave; QSPWs: Quasi-Stationary Planetary Waves; SABER: Sounding of the Atmosphere using Broadband Emission Radiometry; SD: Specified Dynamics; SH: Southern Hemisphere; SSW: Sudden Stratospheric Warming; SW1: Nonmigrating Solar Semidiurnal Westward Wave-1; SW2: Migrating Solar Semidiurnal Tide; SW3: Migrating Solar Semidiurnal Westward Wave-3; TIMED: Thermosphere Ionosphere Mesosphere Energetic and Dynamics; TW3: Migrating Solar Terdiurnal Tide; UT: Universal Time; WACCM-X: Whole Atmosphere Community Climate Model with thermosphere and ionosphere extension; ZMW: Zonal-Mean Zonal Winds.

Acknowledgements

For this work, TAS acknowledges support by Alexander von Humboldt Foundation's Fellowship for Postdoctoral Researchers. This work was partially supported by the Deutsche Forschungsgemeinschaft (DFG, German Research Foundation) under SPP 1788 (DynamicEarth)-CH 1482/1-2 (DYNAMITE2). This material is also partially based upon work supported by the National Center for Atmospheric Research, which is a major facility sponsored by the National Science Foundation under Cooperative Agreement No. 1852977. The authors thank the TIMED/SABER team for the temperature measurements and the availability of the data set at <http://saber.gats-inc.com/>.

Author contributions

TAS, JLC, CS, and YY contributed to the design and implementation of the research, to the analysis of the results and to the writing of the manuscript. All authors read and approved the final manuscript.

Funding

Open Access funding enabled and organized by Projekt DEAL. TAS was supported by postdoctoral fellowship from Alexander von Humboldt Foundation and JLC by Deutsche Forschungsgemeinschaft (1428/1-2, Dynamite2).

Declarations

Availability of data and materials

The SABER kinetic temperature data analysed during the current study are available at <http://saber.gats-inc.com/index.php>. The SD-WACCM-X simulations used in this study can be downloaded from www.earthsystemgrid.org.

Competing interests

The authors declare that they have no competing interests.

Author details

¹Leibniz Institute of Atmospheric Physics at the University of Rostock, Kühlungsborn, Germany. ²GFZ German Research Centre for Geosciences, Potsdam, Germany. ³Present Address: Leibniz Institute of Atmospheric Physics at the University of Rostock, Kühlungsborn, Germany.

Received: 16 February 2022 Accepted: 9 June 2022

Published online: 24 June 2022

References

- Andrews DG, Holton JR, Leovy CB (1987) Middle atmosphere dynamics, vol 40. Academic Press, San Diego
- Baldwin MP, Ayarzagüena B, Birner T, Butchart N, Butler AH, Charlton-Perez AJ, et al (2021) Sudden stratospheric warmings. *Rev Geophys* 59: e2020RG000708. <https://doi.org/10.1029/2020RG000708>
- Butler AH, Seidel DJ, Hardiman SC, Butchart N, Birner T, Match A (2015) Defining sudden stratospheric warmings. *Bull Am Meteorol Soc* 96(11):1913–1928. <https://doi.org/10.1175/BAMS-D-13-00173.1>
- Charney JG, Drazin PG (1961) Propagation of planetary-scale disturbances from the lower into the upper atmosphere. *J Geophys Res* 66(1):83–109. <https://doi.org/10.1029/JZ066i001p00083>
- Chandran A, Collins RL, Garcia RR, Marsh DR (2011) A case study of an elevated stratosphere generated in the whole atmosphere community climate model. *Geophys Res Lett*. 38:L08804. <https://doi.org/10.1029/2010GL046566>
- Charlton AJ, Polvani LM (2007) A new look at stratospheric sudden warmings. Part I: Climatology and modeling benchmarks. *J Clim* 20(3):449–469
- Chau JL, Fejer BG, Goncharenko LP (2009) Quiet variability of equatorial E x B drifts during a sudden stratospheric warming event. *Geophys Res Lett*. 36:L05101. <https://doi.org/10.1029/2008GL036785>
- Chau JL, Goncharenko LP, Fejer BG, Liu H-L (2012) Equatorial and low latitude ionospheric effects during sudden stratospheric warming events. *Space Sci Rev* 168:385–417. <https://doi.org/10.1007/s11214-011-9797-5>
- Chau JL, Hoffmann P, Pedatella NM, Matthias V, Stober G (2015) Upper mesospheric lunar tides over middle and high latitudes during sudden stratospheric warming events. *J Geophys Res Space Phys* 120:3084–3096. <https://doi.org/10.1002/2015JA020998>
- Chen X, Hu X, Xiao C (2012) Variability of MLT winds and waves over mid-latitude during the 2000/2001 and 2009/2010 winter stratospheric sudden warming. *Ann Geophys*. 30:991–1001. <https://doi.org/10.5194/angeo-30-991-2012>
- Fejer BG, Olson ME, Chau JL, Stolle C, Lühr H, Goncharenko LP, Nagatsuma T (2010) Lunar-dependent equatorial ionospheric electrodynamic effects during sudden stratospheric warmings. *J Geophys Res* 115:A00G03. <https://doi.org/10.1029/2010JA015273>
- Forbes JM, Wu D (2006) Solar tides as revealed by measurements of mesosphere temperature by the MLS experiment on UARS. *J Atmos Sci* 63(7):1776–1797. <https://doi.org/10.1175/JAS3724.1>
- Forbes JM, Zhang X (2012) Lunar tide amplification during the January 2009 stratosphere warming event: Observations and theory. *J Geophys Res* 117:A12312. <https://doi.org/10.1029/2012JA017963>
- Forbes JM, Zhang X, Palo S, Russell J, Mertens CJ, Mlynczak M (2008) Tidal variability in the ionospheric dynamo region. *J Geophys Res* 113:A02310. <https://doi.org/10.1029/2007JA012737>
- Fuller-Rowell T, Wu F, Akmaev R, Fang TW, Araujo-Pradere E (2010) A whole atmosphere model simulation of the impact of a sudden stratospheric warming on thermosphere dynamics and electrodynamics. *J Geophys Res* 115:A00G08. <https://doi.org/10.1029/2010JA015524>
- Funke B, López-Puertas M, Bermejo-Pantaleón D, García-Comas M, Stiller GP, von Clarmann T, Kiefer M, Linden A (2010) Evidence for dynamical coupling from the lower atmosphere to the thermosphere during a major stratospheric warming. *Geophys Res Lett*. 37:L13803. <https://doi.org/10.1029/2010GL043619>

- Gan Q, Du J, Ward WE et al (2014) Climatology of the diurnal tides from eCMAM30 (1979 to 2010) and its comparison with SABER. *Earth Planet Space* 66:103. <https://doi.org/10.1186/1880-5981-66-103>
- Gelaro R, McCarty W, Suárez MJ, Todling R, Molod A, Takacs L, Randles CA, Darmenov A, Bosilovich MG, Reichle R, Wargan K, Coy L, Cullather R, Draper C, Akella S, Buchard V, Conaty A, da Silva AM, Gu W, Kim G, Koster R, Lucchesi R, Merkova D, Nielsen JE, Partyka G, Pawson S, Putman W, Rienecker M, Schubert SD, Sienkiewicz M, Zhao B (2017) The modern-era retrospective analysis for research and applications, Version 2 (MERRA-2). *J Clim* 30(14):5419–5454. <https://doi.org/10.1175/JCLI-D-16-0758.1>
- Goncharenko L, Zhang S-R (2008) Ionospheric signatures of sudden stratospheric warming: Ion temperature at middle latitude. *Geophys Res Lett.* 35:L21103. <https://doi.org/10.1029/2008GL035684>
- Goncharenko LP, Coster AJ, Chau JL, Valladares CE (2010) Impact of sudden stratospheric warmings on equatorial ionization anomaly. *J Geophys Res* 115, A00G07. <https://doi.org/10.1029/2010JA015400>
- Goncharenko LP, Coster AJ, Plumb RA, Domeisen DIV (2012) The potential role of stratospheric ozone in the stratosphere-ionosphere coupling during stratospheric warmings. *Geophys Res Lett* 39:L08101. <https://doi.org/10.1029/2012GL051261>
- Gong Y, Ma Z, Lv X, Zhang S, Zhou Q, Aponte N, Sulzer M (2018) A study on the quarterdiurnal tide in the thermosphere at Arecibo during the February 2016 sudden stratospheric warming event. *Geophys Res Lett* 45:13142–13149. <https://doi.org/10.1029/2018GL080422>
- Hays PB, Wu D L (1994). Observations of the diurnal tide from space. *J Atmos Sci* 1994, 51(20),3077–3093. [https://doi.org/10.1175/1520-0469\(1994\)051<\\$<3077:Ootdtf\\$>\\$2.0](https://doi.org/10.1175/1520-0469(1994)051<$<3077:Ootdtf$>$2.0)
- He M, Forbes JM, Chau JL, Li G, Wan W, Korotyshkin DV (2020) High-order solar migrating tides quench at SSW onsets. *Geophys Res Lett.* 47:e2019GL086778. <https://doi.org/10.1029/2019GL086778>
- Hoffmann P, Singer W, Keuer D (2002) Variability of the mesospheric wind fields at middle and Arctic latitudes in winter and its relation to stratospheric circulation disturbances. *J Atmos Sol Terr Phys.* 64:1229–1240
- Hoffmann P, Singer W, Keuer D, Hocking WK, Kunze M, Murayama Y (2007) Latitudinal and longitudinal variability of mesospheric winds and temperatures during stratospheric warming events. *J Atmos Sol Terr Phys.* 69:2355–2366
- Holton JR (1983) The influence of gravity wave breaking on the general circulation of the middle atmosphere. *J Atmos Sci.* 40:2497–2507
- Hurrell JW, Holland MM, Gent PR, Ghan S, Kay JE, Kushner PJ, Lamarque J-F, Large WG, Lawrence D, Lindsay K, Lipscomb WH, Long MC, Mahowald N, Marsh DR, Neale RB, Rasch P, Vavrus S, Vertenstein M, Bader D, Collins WD, Hack JJ, Kiehl J, Marshall S (2013) The community earth system model: a framework for collaborative research. *Bull Am Meteorol Soc* 94(9):1339–1360. <https://doi.org/10.1175/BAMS-D-12-00121.1>
- Hurwitz MM, Newman PA, Garfinkel CI (2011) The Arctic vortex in March 2011: a dynamical perspective. *Atmos Chem Phys.* 11:11447–11453. <https://doi.org/10.5194/acp-11-11447-2011>
- Jin H, Miyoshi Y, Pancheva D, Mukhtarov P, Fujiwara H, Shinagawa H (2012) Response of migrating tides to the stratospheric sudden warming in 2009 and their effects on the ionosphere studied by a whole atmosphere-ionosphere model GAIA with COSMIC and TIMED/SABER observations. *J Geophys Res.* 117:A10323. <https://doi.org/10.1029/2012JA017650>
- Karlsson B, McLandress C, Shepherd TG (2009) Inter-hemispheric mesospheric coupling in a comprehensive middle atmosphere model. *J Atmos Sol Terr Phys.* 71:518–530. <https://doi.org/10.1016/j.jastp.2008.08.006>
- Körnlich H, Becker E (2010) A simple model for the interhemispheric coupling of the middle atmosphere circulation. *Adv Space Res* 45:661–668. <https://doi.org/10.1016/j.asr.2009.11.001>
- Kumari K, Oberheide J (2020) QBO, ENSO and solar cycle effects in short-term nonmigrating tidal variability on planetary wave timescales from SABER - an information-theoretic approach. *J Geophys Res Atmos* 125:e2019JD031910. <https://doi.org/10.1029/2019JD031910>
- Labitzke K (1972) Temperature changes in the mesosphere and stratosphere connected with circulation changes in winter. *J Atmos Sci.* 29:756–766. [https://doi.org/10.1175/1520-0469\(1972\)029<0756:TCITMA>2.0.CO;2](https://doi.org/10.1175/1520-0469(1972)029<0756:TCITMA>2.0.CO;2)
- Labitzke K (1981) Stratospheric-mesospheric midwinter disturbances—a summary of observed characteristics. *J Geophys Res* 86(NC10):9665–9678. <https://doi.org/10.1029/JC086iC10p09665>
- Lieberman RS (1991) Nonmigrating diurnal tides in the equatorial middle atmosphere. *J Atmos Sci.* 48:1112–1123
- Lieberman RS, Oberheide J, Talaat ER (2013) Nonmigrating diurnal tides observed in global thermospheric winds. *J Geophys Res Space Phys* 118:7384–7397. <https://doi.org/10.1002/2013JA018975>
- Lieberman RS, Riggan DM, Ortland DA, Oberheide J, Siskind DE (2015) Global observations and modeling of nonmigrating diurnal tides generated by tide-planetary wave interactions. *J Geophys Res Atmos.* 120:11419–11437. <https://doi.org/10.1002/2015JD023739>
- Limpasuvan V, Richter JH, Orsolini YJ, Stordal F, Kvisel O (2012) The roles of planetary and gravity waves during a major stratospheric sudden warming as characterized in WACCM. *J Atmos Sol-Terr Phys* 78–79:84–98. <https://doi.org/10.1016/j.jastp.2011.03.004>
- Lin CH, Lin JT, Chang LC, Chen WH, Chen CH, Liu JY (2013) Stratospheric sudden warming effects on the ionospheric migrating tides during 2008–2010 observed by FORMOSAT-3/COSMIC. *J Atmos Solar Terr Phys* 103:66–75. <https://doi.org/10.1016/j.jastp.2013.03.026>
- Lindzen RS, Chapman S (1969) Atmospheric tides. *Space Sci Rev* 10(1):3–188
- Liu H-L, Roble RG (2002) A study of a self-generated stratospheric sudden warming and its mesospheric-lower thermospheric impacts using the coupled TIME-GCM/CCM3. *J Geophys Res Atmos.* 107:4695. <https://doi.org/10.1029/2001JD001533>
- Liu HL, Wang W, Richmond AD, Roble RG (2010) Ionospheric variability due to planetary waves and tides for solar minimum conditions. *J Geophys Res Space* 115: A00G01. <https://doi.org/10.1029/2009JA015188>
- Liu HL, Bardeen CG, Foster BT, Lauritzen P, Liu J, Lu G, Marsh DR, Maute A, McInerney JM, Pedatella NM, Qian L, Richmond AD, Roble RG, Solomon SC, Vitt FM, Wang W (2018) Development and validation of the Whole Atmosphere Community Climate Model with thermosphere and ionosphere extension (WACCM-X 2.0). *J Adv Model Earth Syst* 10:381–402. <https://doi.org/10.1002/2017MS001232>
- Liu G, Lieberman RS, Harvey VL, Pedatella NM, Oberheide J, Hibbins RE, et al (2021) Tidal variations in the mesosphere and lower thermosphere before, during, and after the 2009 sudden stratospheric warming. *J Geophys Res Space Phys* 126, e2020JA028827. <https://doi.org/10.1029/2020JA028827>
- Lu X, Liu H-L, Liu AZ, Yue J, McInerney JM, Li Z (2012) Momentum budget of the migrating diurnal tide in the Whole Atmosphere Community Climate Model at vernal equinox. *J Geophys Res.* 117:D07112. <https://doi.org/10.1029/2011JD017089>
- Manney GL, Krüger K, Pawson S, Minschwaner K, Schwartz MJ, Daffer WH, Waters JW (2008) The evolution of the stratosphere during the 2006 major warming: Satellite data and assimilated meteorological analyses. *J Geophys Res* 113:D11115. <https://doi.org/10.1029/2007JD009097>
- Manney GL, Schwartz MJ, Krüger K, Santee ML, Pawson S, Lee JN, Livesey NJ (2009) Aura Microwave Limb Sounder observations of dynamics and transport during the record-breaking, (2009) Arctic stratospheric major warming. *Geophys Res Lett* 36:L12815. <https://doi.org/10.1029/2009GL038586>
- Marsh DR, Mills MJ, Kinnison DE, Lamarque J-F, Calvo N, Polvani LM (2013) Climate change from 1850 to 2005 simulated in CESM1 (WACCM). *J Clim* 26(19):7372–7391. <https://doi.org/10.1175/JCLI-D-12-00558.1>
- Matsuno T (1971) A dynamical model of the stratospheric sudden warming. *J Atmos Sci* 28(8):1479–1494. [https://doi.org/10.1175/1520-0469\(1971\)028<1479:ADMOTS>2.0.CO;2](https://doi.org/10.1175/1520-0469(1971)028<1479:ADMOTS>2.0.CO;2)
- Matthias V, Dörnbrack A, Stober G (2016) The extraordinarily strong and cold polar vortex in the early northern winter 2015/2016. *Geophys Res Lett.* 43:12287–12294. <https://doi.org/10.1002/2016GL071676>
- McLandsress C (2002) The seasonal variation of the propagating diurnal tide in the mesosphere and lower thermosphere. Part II: the role of tidal heating and zonal mean winds. *J Atmos Sci* 59(5): 907–922. [https://doi.org/10.1175/1520-0469\(2002\)059<\\$<0907:TSVOTPS\\$>\\$2.0.CO;2](https://doi.org/10.1175/1520-0469(2002)059<$<0907:TSVOTPS$>$2.0.CO;2)
- Mukherjee BK, Indira K, Dani KK (1987) Perturbations in tropical middle atmosphere during winter. *Meteorol Atmos Phys* 37:17–26
- Oberheide J, Hagan ME, Ward WE, Riese M, Offermann D (2000) Modeling the diurnal tide for the CRISTA-1 time period. *J Geophys Res.* 105:24917–24929
- Oberheide J, Hagan ME, Roble RG, Offermann D (2002) Sources of non-migrating tides in the tropical middle atmosphere. *J Geophys Res.* 107(D21):4567. <https://doi.org/10.1029/2002JD002220>
- Oberheide J, Hagan ME, Roble RG (2003) Tidal signatures and aliasing in temperature data from slowly precessing satellites. *J Geophys Res.* 108:1055. <https://doi.org/10.1029/2002JA009585>

- Pancheva D, Mukhtarov P, Mitchell NJ, Andonov B, Merzlyakov E, Singer W, Murayama Y, Kawamura S, Xiong J, Wan W, Hocking W, Fritts D, Riggins D, Meek C, Manson A (2008) Latitudinal wave coupling of the stratosphere and mesosphere during the major stratospheric warming in 2003/2004. *Ann Geophys*. 26:467–483. <https://doi.org/10.5194/angeo-26-467-2008>
- Pancheva D, Mukhtarov P (2011) Atmospheric tides and planetary waves: Recent progress based on SABER/TIMED temperature measurements (2002–2007). *Aeronomy of the Earth's Atmosphere and Ionosphere*, pp.19–56
- Pedatella NM, Liu HL, Richmond AD, Maute A, Fang T-W (2012) Simulations of solar and lunar tidal variability in the mesosphere and lower thermosphere during sudden stratosphere warmings and their influence on the low-latitude ionosphere. *J Geophys Res* 117:A08326. <https://doi.org/10.1029/2012JA017858>
- Pedatella NM, Liu H-L (2013) The influence of atmospheric tide and planetary wave variability during sudden stratosphere warmings on the low latitude ionosphere. *J Geophys Res Space Phys* 118:5333–5347. <https://doi.org/10.1002/jgra.50492>
- Pedatella NM et al (2014a) The neutral dynamics during the 2009 sudden stratosphere warming simulated by different whole atmosphere models. *J Geophys Res Space Phys* 119:1306–1324. <https://doi.org/10.1002/2013JA019421>
- Pedatella NM, Raeder K, Anderson JL, Liu H-L (2014b) Ensemble data assimilation in the whole atmosphere community climate model. *J Geophys Res Atmos*. 119:9793–9809. <https://doi.org/10.1002/2014JD021776>
- Pedatella NM, Oberheide J, Sutton EK, Liu H-L, Anderson JL, Raeder K (2016) Short-term nonmigrating tide variability in the mesosphere, thermosphere, and ionosphere. *J Geophys Res Space Phys* 121:3621–3633. <https://doi.org/10.1002/2016JA022528>
- Pedatella N, Chau J, Schmidt H, Goncharenko L, Stolle C, Hocke K, Siddiqui T (2018) How sudden stratospheric warming affects the whole atmosphere. *Eos* 99:35–38. <https://doi.org/10.1029/2018EO092441>
- Pedatella NM, Liu H-L, Marsh DR, Raeder K, Anderson JL (2019) Error growth in the mesosphere and lower thermosphere based on Hindcast experiments in a whole atmosphere model. *Space Weather* 17:1442–1460. <https://doi.org/10.1029/2019SW002221>
- Qian L, Burns AG, Emery BA, Foster B, Lu G, Maute A, Richmond AD, Roble RG, Solomon SC, Wang W (2014) The NCAR TIE-GCM: A community model of the coupled thermosphere/ionosphere system, in *Modeling the Ionosphere-Thermosphere System*, AGU Geophysical Monograph Series
- Remsberg EE, Marshall BT, Garcia-Comas M, Krueger D, Lingenfeller GS, Martin-Torres J et al (2008) Assessment of the quality of the Version 1.07 temperature-versus-pressure profiles of the middle atmosphere from TIMED/SABER. *J Geophys Res* 113: D17101. <https://doi.org/10.1029/2008JD010013>
- Richmond AD, Ridley EC, Roble RG (1992) A thermosphere/ionosphere general circulation model with coupled electrodynamics. *Geophys Res Lett*. 6:601–604. <https://doi.org/10.1029/92GL00401>
- Sabine E (1847) On the lunar atmospheric tide at St. Helena. *Philos Trans Royal Soc London* 137:45–50. <https://doi.org/10.1098/rstl.1847.0005>
- Salby ML (1982) Sampling theory for synoptic satellite observations. Part I: Space-time spectra, resolution, and aliasing. *J Atmos Sci* 39:2577–2601
- Sassi F, Liu H-L, Ma J, Garcia RR (2013) The lower thermosphere during the northern hemisphere winter of 2009: A modeling study using high-altitude data assimilation products in WACCM-X. *J Geophys Res Atmos*. 118:8954–8968. <https://doi.org/10.1002/jgrd.50632>
- Sathishkumar S, Sridharan S, Jacobi C (2009) Dynamical response of low-latitude middle atmosphere to major sudden stratospheric warming events. *J Atmos Solar Terr Phys* 71:857–865. <https://doi.org/10.1016/j.jastp.2009.04.002>
- Scherhag R (1952) Die explosionsartigen stratosphärenwärmungen des spätwinters 1951/52. *Berichte des deutschen Wetterdienstes in der US-Zone* 6(38):51–63
- Shepherd MG, Wu DL, Fedulina IN, Gurubaran S, Russell JM, Mlynczak MG, Shepherd GG (2007) Stratospheric warming effects on the tropical mesospheric temperature field. *J Atmos Solar Terrestrial Phys* 69:2309–2337. <https://doi.org/10.1016/j.jastp.2007.04.009>
- Siddiqui TA, Stolle C, Lühr H, Matzka J (2015) On the relationship between weakening of the northern polar vortex and the lunar tidal amplification in the equatorial electrojet. *J Geophys Res Space Phys* 120:10006–10019. <https://doi.org/10.1002/2015JA021683>
- Siddiqui TA, Maute A, Pedatella NM (2019) On the importance of interactive ozone chemistry in Earth-System models for studying mesosphere-lower thermosphere tidal changes during sudden stratospheric warmings. *J Geophys Res Space Phys* 124(12):10690–10707. <https://doi.org/10.1029/2019JA027193>
- Singh D, Gurubaran S (2017) Variability of diurnal tide in the MLT region over Tirunelveli (8.7°N), India: Consistency between ground- and space-based observations. *J Geophys Res Atmos*. 122:2696–2713. <https://doi.org/10.1002/2016JD025910>
- Siskind DE, Eckermann SD, Coy L, McCormack JP, Randall CE (2007) On recent interannual variability of the Arctic winter mesosphere: implications for tracer descent. *Geophys Res Lett*. 34:L09806. <https://doi.org/10.1029/2007GL029293>
- Siskind DE, Eckermann SD, McCormack JP, Coy L, Hoppel KW, Baker NL (2010) Case studies of the mesospheric response to recent minor, major, and extended stratospheric warmings. *J Geophys Res* 115: D00N03. <https://doi.org/10.1029/2010JD014114>
- Sridharan S (2017) Variabilities of low-latitude migrating and nonmigrating tides in GPS-TEC and TIMED-SABER temperature during the sudden stratospheric warming event of 2013. *J Geophys Res Space Phys* 122:10748–10761. <https://doi.org/10.1002/2017JA024283>
- Sridharan S, Tsuda T, Gurubaran S (2010) Long-term tendencies in the mesosphere/lower thermosphere mean winds and tides as observed by medium frequency radar at Tirunelveli (8.7°N, 77.8°E). *J Geophys Res*. 115:D08109. <https://doi.org/10.1029/2008JD011609>
- Vincent RA, Kovalam S, Fritts DC, Isler JR (1998) Long-term MF radar observations of solar tides in the low-latitude mesosphere: Interannual variability and comparisons with the GSWM. *J Geophys Res-Atmos* 103(D8):8667–8683. <https://doi.org/10.1029/98jd00482>
- Vitharana A, Zhu X, Du J, Oberheide J, Ward WE (2019) Statistical modeling of tidal weather in the mesosphere and lower thermosphere. *J Geophys Res Atmos* 124:9011–9027. <https://doi.org/10.1029/2019JD030573>
- Waugh DW, Polvani LM (2010) Stratospheric polar vortices. In: *The Stratosphere: Dynamics, Transport, and Chemistry*. <https://doi.org/10.1002/9781118666630.ch3>
- WMO/IQSY (1964). International years of the Quiet Sun (IQSY) 1964–65. Alert messages with special references to stratwarms. WMO/IQSY Report No 6, Secretariat of the World Meteorological Organization, Geneva, Switzerland. World Meteorological Organization
- Yamazaki Y, Matthias V, Miyoshi Y, Stolle C, Siddiqui T, Kervalishvili G, Alken P (2020) September 2019 Antarctic sudden stratospheric warming: Quasi-6-day wave burst and ionospheric effects. *Geophys Res Lett*. 47(1): e2019GL086577. <https://doi.org/10.1029/2019GL086577>
- Zhang X, Forbes JM (2014) Lunar tide in the thermosphere and weakening of the northern polar vortex. *Geophys Res Lett* 41(23):8201–8207. <https://doi.org/10.1002/2014GL026103>
- Zhu X, Yee J-H, Talaat ER, Mlynczak M, Gordley L, Mertens C, Russell JM III (2005) An algorithm for extracting zonal mean and migrating tidal fields in the middle atmosphere from satellite measurements: applications to TIMED/SABER measured temperature and tidal modeling. *J Geophys Res*. 110:D02105. <https://doi.org/10.1029/2004JD004996>
- Zuev VV, Savelieva E (2019) The cause of the strengthening of the Antarctic polar vortex during October–November periods. *J Atmos Solar Terrestrial Phys* 190:1–5. <https://doi.org/10.1016/j.jastp.2019.04.016>
- Zülicke C, Becker E (2013) The structure of the mesosphere during sudden stratospheric warmings in a global circulation model. *Res Atmos J Geophys*. <https://doi.org/10.1002/jgrd.50219>
- Zülicke C, Becker E, Matthias V, Peters DHW, Schmidt H, Liu H-L, de la Torre-Ramos L, Mitchell DM (2018) Coupling of stratospheric warmings with mesospheric coolings in observations and simulations. *J Clim* 31:1107–1133. <https://doi.org/10.1175/JCLI-D-17-0047.1>

Publisher's Note

Springer Nature remains neutral with regard to jurisdictional claims in published maps and institutional affiliations.